CONDENSED MATTER PHYSICS

Anomalous Hall effect derived from multiple Weyl nodes in high-mobility $EuTiO_3$ films

Kei S. Takahashi[1,2*†], Hiroaki Ishizuka[3†], Tomoki Murata[3], Qing Y. Wang[1‡], Yoshinori Tokura[1,3], Naoto Nagaosa[1,3], Masashi Kawasaki[1,3]

$EuTiO_3$, a magnetic semiconductor with a simple band structure, is one of the ideal systems to control the anomalous Hall effect (AHE) by tuning the Fermi level. The electrons in the conduction bands of La-doped $EuTiO_3$ are subject to the spin-orbit interaction and Zeeman field from the spontaneous magnetization, which generates rich structures in the electron band such as Weyl nodes. This unique property makes $EuTiO_3$ a relatively simple multiband system with its Berry curvature being controlled by electron doping and magnetic field. We report a nonmonotonic magnetic field dependence of the anomalous Hall resistivity, which is ascribed to the change of electronic bands induced by the Zeeman splitting during the magnetization process. The anomalous Hall resistivity measurement in high-mobility films grown by gas source molecular beam epitaxy shows additional terms in the AHE during the magnetization process, which is not proportional to the magnetization. Our theoretical calculation indicates that the change of Zeeman field in the process of canting the magnetic moments causes the type II Weyl nodes in the conduction band to move, resulting in a peculiar magnetic field dependence of the AHE; this is revealed by the high-quality films with a long scattering lifetime of conduction electrons.

INTRODUCTION

Transport properties of spin-polarized electrons receive considerable interest for their importance in basic science and for their potential in technological applications (*1*). One of the peculiar phenomena of the conduction of spin-polarized electrons in magnetic metals that contains rich physics is the anomalous Hall effect (AHE). Many different mechanisms contribute to the AHE, such as the Berry phase of the electronic bands (*2*), impurity scattering (*3*, *4*), the spin Berry phase (*5*), etc. Among them, one well-studied mechanism is the intrinsic mechanism that is related to the Berry curvature of electronic bands (*2*, *6*), and many experimental results are ascribed to this mechanism (*7*–*13*). In magnetic oxides with complex band structures, the band crossings often affect the Berry curvature, resulting in a complicated distribution of the Berry curvature. In these cases, the AHE is very sensitive to the Fermi level shift around the band crossing points, giving an opportunity to control the AHE by Fermi level tuning such as by carrier doping. In a pioneering work, the sign change of the AHE as a function of temperature was discovered in $SrRuO_3$. This is explained by the change of the total Berry curvature due to Fermi level shifting around the crossing points through the temperature scan (*11*). However, for usual ferromagnetic metals such as $SrRuO_3$, the electronic structure near the Fermi energy is so complicated that theoretical predictions of the trends in the experiment as in $SrRuO_3$ are rare. In contrast, in a recent report, it was discussed that the magnetic semiconductor $EuTiO_3$ (ETO) has a relatively simple band structure with band crossings (*14*). In addition, the magnetism is dominated by the exchange interaction between the nearest neighbors of Eu. This interaction should be rigid against the tiny amount of substitution of Eu by La. Therefore, the Fermi level can be tuned around the band crossing points while keeping the magnetization almost constant, whereas the Fermi level of $SrRuO_3$ is hardly controlled by carrier doping because of the large amount of carriers. Hence, ETO was considered as an ideal material to study the control of Berry phase and the AHE by tuning the Fermi level (*14*).

As shown in Fig. 1A, ETO is a band insulator with a cubic perovskite structure. The Ti ions are in the tetravalent state, and the Eu ions are in a divalent state; the Eu ions have $4f^7$ ($S = {}^7/_2$) moments that order antiferromagnetically at 5.5 K, while the Ti 3d orbitals are empty in undoped samples. By substituting Eu^{2+} with La^{3+}, electron carriers are introduced into the conduction band of the 3d t_{2g} states. We found that the antiferromagnetic order is kept even for the La-doped ETO films on $(LaAlO_3)_{0.3}(Sr_2AlTaO_6)_{0.7}$ (LSAT) single crystal substrates up to $n = 1.5 \times 10^{20}$ cm^{-3}. By applying a magnetic field, the magnetic order changes from antiferromagnetic to canted antiferromagnetic, and, finally, to ferromagnetic (*15*). Carrier doping up to $n = 1.5 \times 10^{20}$ cm^{-3} does not modify such magnetization behavior. In the electron-doped ETO, the doped Ti 3d electrons contribute to the metallic conduction. In addition, they induce the interactions between localized Eu spins through the RKKY (Ruderman-Kittel-Kasuya-Yosida) mechanism (*16*–*18*); they are expected to be dominantly ferromagnetic.

The lattice constant of ETO (3.905 Å) is larger than that of a LSAT (3.868 Å) substrate. Therefore, in the ETO films on LSAT, the compressive strain is induced in the ETO films because of the difference of lattice constant between ETO and LSAT. Because of this epitaxial compressive strain, two band crossing points between d_{xy} and $d_{yz/zx}$ of t_{2g} orbital bands (they are mixed by the spin orbit interaction (SOI) to form $J_{eff} = {}^3/_2$) appear along the k_z axis near $k = 0$, as pointed out in (*14*). By tuning the Fermi level close to the band crossing with the use of La doping, we successfully elucidated the sign change of the AHE predicted in the previous theoretical calculation. Taking account of the Zeeman splitting between up and down spin bands, each band crossing point splits into four crossing points (Weyl nodes), forming eight Weyl nodes in total. The position of these nodes moves in the Brillouin zone as the Zeeman splitting changes during the magnetization process, namely, spin canting process under the magnetic field. In the previous paper (*14*), such effect could not be resolved as the detailed structure might be smeared because of the broadening of the band for low-mobility films. In contrast, in this report,

[1]RIKEN Center for Emergent Matter Science, Wako 351-0198, Japan. [2]PRESTO, Japan Science and Technology Agency, Chiyoda-ku, Tokyo 102-0075, Japan. [3]Department of Applied Physics and Quantum Phase Electronics Center, University of Tokyo, Tokyo 113-8656, Japan.
*Corresponding author. Email: kei.takahashi@riken.jp
†These authors contributed equally to this work.
‡Present address: National Laboratory for Superconductivity, Beijing National Laboratory for Condensed Matter Physics, Institute of Physics, Chinese Academy of Sciences, Beijing100190, China.

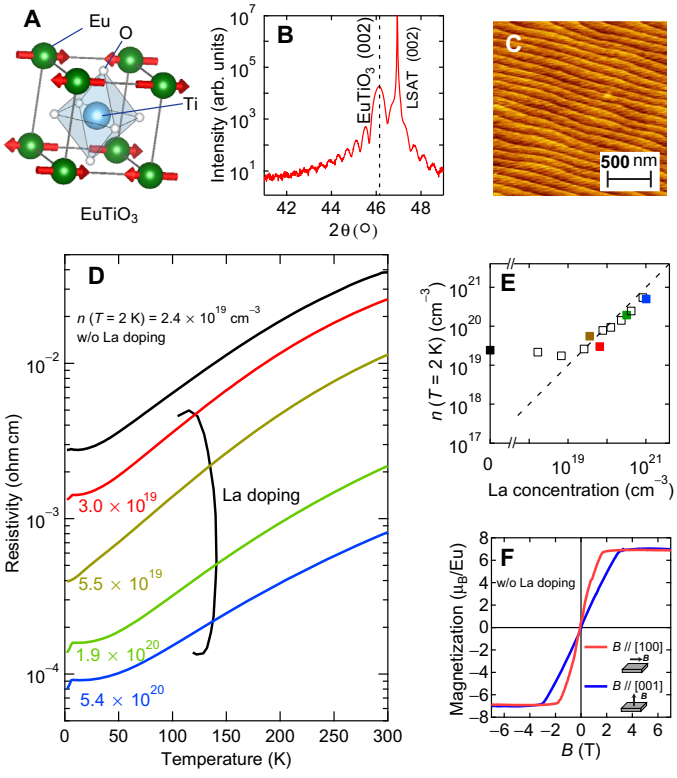

Fig. 1. Structure and basic properties of $EuTiO_3$ (ETO) films. (**A**) A schematic of the crystal structure. (**B**) 2θ-θ x-ray diffraction pattern around (002) peaks for an ETO thin film on an LSAT substrate. (**C**) An AFM image (2 × 2 μm^2) for the surface of an ETO film. (**D**) Temperature dependence of resistivity for ETO films with various carrier densities (*n*). (**E**) Relation between the carrier density *n* and nominal La concentration for ETO films. (**F**) Magnetization curves at 2 K for an ETO film with $n = 2.4 \times 10^{19}$ cm^{-3}. The magnetic field is applied along in-plane [100] (red) and out-of-plane [001] (blue) axes.

by examining higher-mobility films than the films previously reported, we elucidate a peculiar behavior of the AHE associated with the change of electronic bands by Zeeman splitting.

Recently, high–crystalline quality complex oxide films were grown by metalorganic (MO) gas-source molecular beam epitaxy (MBE). For example, a La-doped $SrTiO_3$ (STO) film shows very high mobility exceeding the maximum mobility of a bulk single crystal (22,000 cm^2 V^{-1}s^{-1}) (*19*), and quantum Hall effect was successfully observed in the two-dimensional (2D) electron gas of δ-doped STO grown at high temperature by MOMBE (*20*). Therefore, $EuTiO_3$ films with higher mobility than pulsed laser deposition (PLD) films are expected by the MOMBE. In the case of PLD films, the large energy broadening of conduction bands due to the short scattering time might mask the fine structure of the bands, which would contribute to the AHE. Therefore, the MOMBE films with longer scattering time may reveal the additional character of magnetotransport, which was hidden in PLD films. Thus, it is worth investigating the transport properties of the high-mobility ETO films that can be fabricated by MOMBE.

RESULTS

Experiments

Single-crystalline films of La-doped $EuTiO_3$ (ETO) were grown at 900°C by MOMBE on cubic LSAT (001) substrates with nominal La concentrations varied from 0 to 2.2×10^{20} cm^{-3}. The thickness of all the films was fixed at around 25 nm. Figure 1B shows a 2 θ-θ scan of an ETO film around the (002) peaks. A sharp (002) film peak and clear Laue's fringes can be seen, indicating the high crystalline quality. The in-plane lattice of the films is coherently matched with that of the substrate a = 3.868 Å. The *c*-axis lattice constant is deduced as 3.931 Å (c/a = 1.016), which is slightly smaller than that of PLD films (3.940 Å, c/a = 1.019) as previously reported. The strain $\varepsilon = \left(\frac{(a_{||} - a_0)}{a_0}\right)$ is estimated as −0.95%, where a_0 is the lattice constant of bulk single-crystal $EuTiO_3$ (3.905 Å), and $a_{||}$ is the in-plane lattice constant of a $EuTiO_3$ film coherently locked with an LSAT substrate (3.868 Å). As in the cases of the $SrTiO_3$ and $BaTiO_3$ film grown by the same method, the lattice constant deviates from the proper value when the nonstoichiometry exists (*21*). With varying the beam flux ratio between titanium tetra isopropoxide (TTIP) as Ti precursor and Eu, the ratio was optimized, as shown in figs. S1 and S2. Eventually, we found that MBE films discussed here are stoichiometric, but PLD films are not. This small difference in *c*-axis lattice constant and tetragonality should cause the difference in the energy splitting between the *xy* orbital and the *yz*/*zx* orbitals. An atomic force microscope (AFM) image of the film is shown in Fig. 1C, exhibiting a step-and-terrace structure. The step height is approximately 4 Å, corresponding to the height of a single ETO unit cell. Figure 1D shows the temperature dependence of resistivity for the ETO films. As La doping increases, resistivity systematically decreases. At around 5.5 K, kink structures are observed. The temperature dependences of magnetization also show kink structures at around 5.5 K, corresponding to the Néel temperature, as shown in fig. S3. This indicates that the spin ordering of Eu correlates with the scattering of the conduction electrons. The relationship between the carrier density *n* and the La concentration is shown in Fig. 1E; *n* is determined from the slope of the ordinary Hall effect term at 2 K, and the La density is estimated by the flux measured by a quartz crystal microbalance. As mentioned in Materials and Methods, all the films grown under the reductive condition contain oxygen defects. Thus, the nondoped film is not an insulator but exhibits metallic behavior with electron carriers ($n \sim 2.4 \times 10^{19}$ cm^{-3}), and carrier density *n* can be controlled by La doping at higher doping levels than 2.4×10^{19} cm^{-3} as the dashed line in Fig. 1E indicates. We note that the *c*-axis lattice constants of all the films are almost identical as 3.931 ± 0.002 Å, suggesting that similar amounts of oxygen vacancies are incorporated in the films regardless of the La doping level (*22*). Figure 1F shows the magnetization curves at 2 K. The magnetic field is applied along in-plane and out-of-plane axes. As previously reported, the absence of remanent magnetization at zero field indicates an antiferromagnetic ordering. The magnetization increases and saturates at 7 μ_B per Eu by applying a magnetic field of B = 1.8 T along an in-plane axis and B = 3 T along an out-of-plane axis. The saturation moment 7 μ_B per Eu coincides with the full spin moment of Eu^{2+} ($4f^7$), and such anisotropy can be explained by a demagnetizing field effect of the thin-film form.

Next, we discuss the transport properties in detail. Figure 2A shows the Hall resistivity (ρ_H) for the ETO film as a function of magnetic field at 2 K. ρ_H is expressed as

$$\rho_H = R_H B + \rho_{AHE}$$

where R_H is the ordinary Hall coefficient and ρ_{AHE} is the anomalous Hall resistivity, which would have been proportional to the magnetization in conventional magnetic systems. The dashed line is the linear fit with the slope of ρ_H above 3 T (the saturation magnetic field), corresponding to the ordinary term ($R_H B$). By subtracting the linear

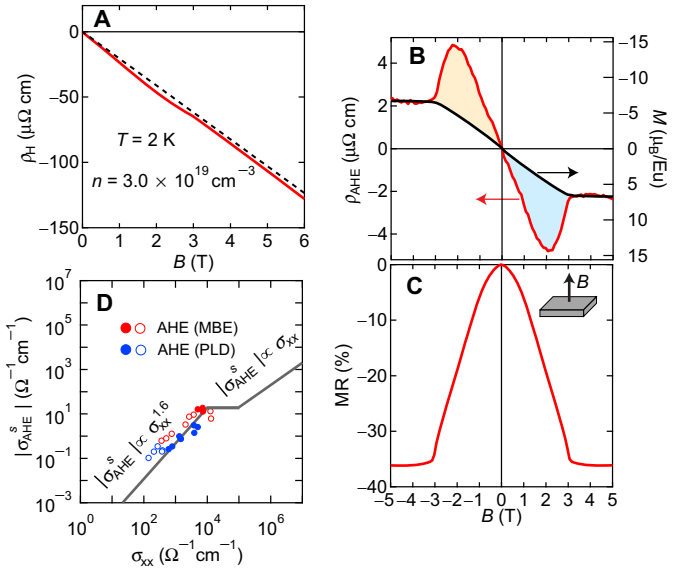

Fig. 2. Magnetotransport properties of $EuTiO_3$ films. (**A**) Magnetic field dependence of Hall resistivity (ρ_H) for the ETO film with $n = 3.0 \times 10^{19}$ cm^{-3}. The dashed line is the linear fit with the slope of ρ_H above 3 T (the saturation magnetic field), corresponding to the ordinary Hall effect term (R_HB). (**B**) AHE at 2 K for the ETO film as a function of the magnetic field after subtraction of ordinary Hall effect term. (**C**) MR at 2 K for the ETO film as a function of magnetic field. (**D**) Relationship between the magnitude of anomalous Hall conductivity (σ^s_{xy}) and the longitudinal conductivity (σ_{xx}) at 2 K for ETO films. The polyline depicts the universal relation of anomalous Hall conductivity $|\sigma^s_{AHE}|$ with σ_{xx}: The AHE is caused by the Berry phase mechanism regime suppressed by the disorder ($|\sigma^s_{AHE}| \propto \sigma^{\alpha=1.6}_{xx}$), the so-called intrinsic AHE ($|\sigma^s_{AHE}|$ = constant), and the skew-type scattering, namely, extrinsic AHE ($|\sigma^s_{AHE}| \propto \sigma^{\alpha=1.0}_{xx}$). Red (blue) symbols are for those grown by MBE in this study [PLD in a previous study (*14*)]. Solid (open) symbols stand for positive (negative).

ordinary term from the ρ_H, the anomalous term was extracted, as shown in Fig. 2B. The carrier density for each film is determined using the R_H. To be precise, the part of the ρ_H curve above 3 T in Fig. 2A is not perfectly linear. The fitting error is about 5%, resulting in the same order of that for the carrier density. Presumably, the tiny deviation from the linear function is related to the magnetic field dependence of the magnetic moment derived from 3d conduction electrons or to the multiband nature of the t_{2g} orbitals. The magnetization curve is also plotted on the right axis to scale both the values of the magnetization and ρ_{AHE} above 3 T in saturation. For the following discussions, the saturation value of ρ_{AHE} is defined as ρ^s_{AHE}. Note that there is a large additional component of the AHE shaded by blue and orange colors deviating from the curve of magnetization below saturation field, which will be discussed later. We could find such an unconventional component below the saturation field in the anomalous Hall conductivity $\sigma_{AHE}(B)$ curves deduced from $\rho_{AHE}(B)$ and $\rho_{xx}(B)$ as well. Typical data for four carrier density samples are shown in fig. S4. Note that the nonmonotonic behavior of the AHE is observed not only in La-doped films but also in the film that is doped solely by the oxygen vacancy. Figure 2C shows the magnetoresistance (MR) of the film. During the magnetization process from 0 to 3 T, a large negative MR appears presumably because of the suppression of the scattering through the spin alignment of Eu. Figure 2D displays σ^s_{AHE} versus σ_{xx} by a log-log plot. Here, σ_{xx} and σ^s_{AHE} are calculated as $\sigma_{xx} = \frac{\rho_{xx}(B=0)}{(\rho^s_{AHE})^2 + \rho_{xx}(B=0)^2}$ and $\sigma^s_{AHE} = \frac{\rho^s_{AHE}}{(\rho^s_{AHE})^2 + \rho_{xx}(B=0)^2}$. Positive (negative) σ^s_{AHE} is plotted as solid (open) circles. It is known that there exist three regimes in the scaling behavior of the AHE depending on the range of σ_{xx}, which are categorized by a scaling parameter, α, in $\sigma^s_{AHE} \propto \sigma^{\alpha}_{xx}$ (*6*, *23*, *24*). (i) $\alpha \sim 1.6$, when σ_{xx} is below 1×10^4 ohm^{-1} cm^{-1}, where the anomalous Hall velocity induced by the Berry curvature of conduction bands is disturbed and suppressed by the disorder; (ii) $\alpha \sim 1.0$ for large σ_{xx} above 1×10^5 ohm^{-1} cm^{-1}, where the AHE is caused by the skew-type scattering, namely, the extrinsic AHE; and (iii) $\alpha \sim 0$ for the intermediate σ_{xx} between (i) and (ii), the so-called intrinsic AHE due to Berry curvature. These scaling laws are denoted as polylines in Fig. 2D. For the ETO films discussed in this study, the carrier density is designed between 2×10^{19} and 1.5×10^{21} cm^{-3}, and all the data obey the scaling $\sigma^s_{AHE} \propto \sigma^{\alpha=1.6}_{xx}$, suggesting that the Berry phase mechanism regime of the AHE is suppressed by the disorder.

To discuss the peculiar anomalous Hall term, the additional component of the AHE ($\Delta\rho_{AHE}$) is defined as $\Delta\rho_{AHE} = \rho_{AHE} - R_sM$, where R_s is determined to be $\Delta\rho_{AHE} = 0$ above 3 T with saturated magnetization. For example, as mentioned above, the $\Delta\rho_{AHE}$ for $n = 3.0 \times 10^{19}$ cm^{-3} corresponds to the shaded component in Fig. 2B. Figure 3 (A and B) shows the magnetic field dependence of $\Delta\rho_{AHE}$ and MR $\left[\text{MR}\ (\%) = \frac{\rho(B) - \rho(B=0)}{\rho(B=0)}\right]$ for ETO films with various carrier densities. Although the magnetization versus magnetic field behaviors are almost the same in this range of carrier density, the saturation magnetic field slightly decreases as the carrier density increases, as indicated by vertical bars in Fig. 3 (A and B). Each bar denotes the saturation magnetic field that is determined by the differential curve of MR. The existence of $\Delta\rho_{AHE}$ at the magnetization process reminds us that a spin texture such as a skyrmion lattice causes a fictitious magnetic field and topological Hall effect, which are realized in B20 compounds (*25*, *26*). Those skyrmion lattices are stabilized by the Dzyaloshinskii-Moriya (DM) interaction arising in noncentrosymmetric crystal structures and interfaces or the competition of long-range dipolar energy in a thin-film geometry and domain wall energy (*27*, *28*). Given that skyrmions exist in the ETO film on the LSAT substrate, those may be caused by DM interaction due to the broken inversion symmetry at the interface. If $\Delta\rho_{AHE}$ were a consequence of the skyrmion formation based on the interface DM interaction, then the sign of the topological Hall effect would be determined by the sign of the normal Hall effect (*29*). Thus, the sign change of topological Hall effect, as observed, could be hardly reconciled with the constant sign (negative) of the charge carrier. In our experiment, however, the sign of $\Delta\rho_{AHE}$ changes twice as the carrier density increases. These sign changes as a function of carrier density cannot be explained by conventional topological Hall effect scenarios. The MR also shows an interesting behavior by changing the carrier density. Although low–carrier density films below 1.4×10^{20} cm^{-3} exhibit negative MR for the magnetization process between 0 and 3 T, positive MR behaviors are seen for high–carrier density films. As mentioned above, the negative MR between the antiferromagnetic state at 0 T and the ferromagnetic spin ordering above 3 T seems to be understood as follows. The scattering time of conduction electrons in ferromagnetic spin texture is longer than that in the antiferromagnetic one. However, such negative to positive change in MR by increasing the carrier density cannot be explained by the conventional scattering time difference. The theoretical approach to the longitudinal MR (R_{xx}) behavior is much more complicated than that to the transverse (Hall) resistance (R_{xy}). Therefore, although we expect that the positive MR might be also related to the Weyl nodes, the origin of the positive MR remains unclear to be studied in future. Here, we focus on the behavior of the Hall effect to which the Berry phase theory can be directly applied.

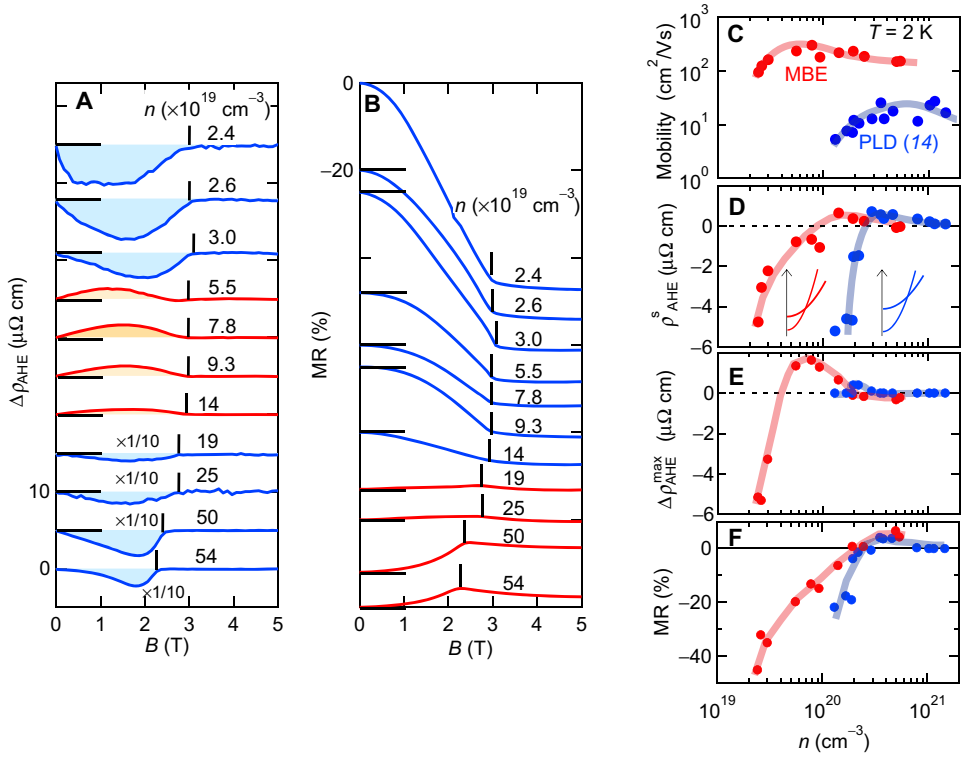

Fig. 3. Carrier density dependence of magnetotransport properties of $EuTiO_3$ films. (**A**) Unconventional term of the AHE ($\Delta\rho_{AHE}$) defined as $\Delta\rho_{AHE} = \rho_{AHE} - R_s M$ and (**B**) MR at 2 K as a function of magnetic field. Vertical bars indicate saturation field defined by the derivative of MR. Curves are vertically offset as denoted by horizontal bars. Carrier density dependence of mobility (**C**), saturation value of ρ_{AHE} (ρ^s_{AHE}) (**D**), maximum value of $\Delta\rho_{AHE}$ (**E**), MR at each saturation field, and (**F**) at 2 K for ETO films. The lines are merely guides to the eye.

To shed light on the carrier density dependence of magnetotransport properties, we show in Fig. 3 (C to F) the mobility, ρ^s_{AHE}, $\Delta\rho^{max}_{AHE}$, and MR at 2 K for MBE and PLD films as a function of carrier density, where $\Delta\rho^{max}_{AHE}$ is the maximum value of $\Delta\rho_{AHE}$ at a magnetic field in Fig. 3A. All data for PLD films measured in the previous report were reanalyzed. Because of the higher crystalline quality of MBE films than that of PLD films, the mobility of electrons in MBE films is one order of magnitude higher than that of PLD films, as shown in Fig. 3C; the maximum value reaches 300 $cm^2\ V^{-1}\ s^{-1}$ at 2 K. Thus, the scattering time of MBE films becomes longer, and the energy broadening of conduction bands must be smaller than that of PLD films. In Fig. 3D, the sign change of ρ^s_{AHE} from negative to positive occurs at around 1×10^{20} cm^{-3} for the MBE films, whereas it occurs around 2×10^{20} cm^{-3} for PLD films. Such a sign change for PLD films was already explained in the previous paper (*14*). The sign change occurs at the carrier density where the Fermi energy is around the band crossing point that is formed by the orbital band lifting because of the tetragonal distortion in the epitaxially strained film. As mentioned above, the tetragonal lattice distortion of MBE films is smaller than that of PLD films. This might cause the smaller energy splitting of t_{2g} orbitals for MBE films, resulting in the lower energy where the band crossing occurs in *k*-space, as shown by inset schematics. Accordingly, the carrier density dependence of ρ^s_{AHE} for MBE films shifts to the lower carrier density side than that for PLD films. The sign of $\Delta\rho^{max}_{AHE}$ for MBE films changes twice from 2×10^{19} to 5×10^{20} cm^{-3}. For MR of MBE and PLD films, the sign change can be seen around 1.6×10^{20} cm^{-3} from negative to positive as the carrier density increases. These behaviors of ρ^s_{AHE}, $\Delta\rho^{max}_{AHE}$, and MR as a function of carrier density seem to correlate with each other.

Theory

The above observations suggest that the unconventional behavior of the anomalous Hall resistivity $\Delta\rho_{AHE}$ is also related to the band crossings of the conduction electrons. To provide further insight into the nonmonotonic behavior of the AHE, we next turn to the theoretical analysis of the AHE. In ETO, the conduction bands consist of the 3d orbitals of Ti ions that split into the t_{2g} and e_g orbitals because of the crystal field; the electrons in t_{2g} orbitals are responsible for the conduction, which form sixfold degeneracy at the Γ point. In the La-doped ETO with the carrier density up to around 1×10^{20} cm^{-3}, the Fermi level is expected to be about 100 meV or less above the band bottom. Because of the low Fermi level, as we will discuss below, the fine structure of the bands due to spin-orbit interaction can give a relevant contribution. Therefore, we also take into account the spin-orbit interaction that further splits the sixfold t_{2g} orbitals at the Γ point into fourfold $J = {}^3/_2$ and twofold $J = {}^1/_2$ states (*30*); we consider an effective four-band model for the $J = {}^3/_2$ orbitals as they have lower energy than the $J = {}^1/_2$ states. For the ETO thin films synthesized by MOMBE, we find small lattice distortion ($c/a = 1.016$) due to the strain from the substrate. Considering the above features, the effective model for the La-doped ETO thin films is constructed by the $k \cdot p$ theory around the Γ point for the $J = {}^3/_2$ bands (*14*). It is given by the Luttinger Hamiltonian with a uniaxial anisotropy term that represents the strain from the substrate (*14*, *31*)

$$H_0(\vec{k}) = t\sum_\alpha k_\alpha^2\left(\frac{1}{4} + \frac{J_\alpha^2}{3}\right) + \frac{\delta t}{3}\sum_{\alpha\neq\beta} k_\alpha k_\beta J_\alpha J_\beta - \frac{V_{tetra}}{3}J_z^2 \qquad (1)$$

Here, J_α ($\alpha = x, y, z$) are the 4×4 spin operators for $J = {}^3/_2$, k_α is the α component of the crystal momentum, and V_{tetra} is the uniaxial anisotropy induced by the strain. We here set the band parameters in the Hamiltonian consistent with that in a preceding work (*14*) (t = 300 meV and $\delta t = -100$ meV), while using a smaller uniaxial distortion, V_{tetra} = 45 meV, as the distortion observed in MBE films is smaller than that in the PLD films (V_{tetra} = 60 meV). In addition to these terms, we consider the coupling of conduction electrons to the magnetic moments of Eu 4f moments via the Zeeman coupling. For the Zeeman coupling, in general, we need to consider the coupling of itinerant electrons to both uniform and the staggered magnetizations. We, however, find that the coupling to the staggered magnetization is not allowed by the symmetry (see Materials and Methods). Therefore, the Hamiltonian for the symmetry-allowed exchange coupling between the Eu 4f localized moments and Ti $J = {}^3/_2$ itinerant electrons reads

$$H_h = \frac{\Delta(h)}{3}\left(J_z \cos\theta + J_z^3 \sin\theta\right) \tag{2}$$

Here, $\Delta(h)$ is the strength of the Zeeman coupling as a function of uniform magnetization h, and $\theta = -\pi/4$ is the parameter that defines the ratio of J_z and J_z^3. θ is a parameter that defines the form of Zeeman coupling (*30*); it is chosen such that the anomalous Hall conductivity becomes consistent with the experiment.

In Fig. 4, we show the theoretical result of anomalous Hall conductivity for the effective Hamiltonian. Figure 4C shows the Zeeman splitting h and the chemical potential μ dependence of the anomalous Hall conductivity σ_{AHE}. The blue shade shows the region with negative σ_{AHE}, and the position of the Weyl nodes at $h = 0$ and $h = h_c$ is shown by the red arrows. In the Luttinger model, the two pairs of Weyl nodes are at energies $E_{\text{W}}^{\pm} = \frac{2}{3}V_{\text{tetra}} \pm \frac{1}{2}h \sin\theta$ and that of double Weyl nodes at $E_{\text{DW}}^{\pm} = \frac{2}{3}V_{\text{tetra}} \mp \frac{1}{8}h(4\cos\theta + 5\sin\theta)$ (see Fig. 5, A to D). For the field $h \le h_c$, all nodes are located in between 21.5 meV $< E_{\text{W,DW}}^{\pm} <$ 38.5 meV, as shown by the arrows. At $h = h_c$, we find a sign change of the anomalous Hall conductivity from negative to positive, consistent with the experiment in Fig. 3D; the comparison of σ_{AHE} to that in the experiment is shown in Fig. 4D. We also find the nonmonotonic behavior of the anomalous Hall conductivity in the wide range of electron density with respect to the external magnetic field. The field dependence of the anomalous Hall conductivity for various chemical potentials with relaxation time $\tau = 2.2 \times 10^{-13}$ s ($\hbar/\tau$ = 3 meV) is shown in Fig. 4A; the same curve is also shown in Fig. 4C by the solid lines on the surface. In the calculation of the Hall conductivity, we used a relaxation time that was somewhat longer than in the previous paper (*14*), as the conductivity in MOMBE films are higher than that in PLD by the enhancement of the mobility. In addition, we here assumed that the major contribution to the Zeeman splitting comes from the coupling of the Eu moments to the Ti electrons. Hence, we assumed the Zeeman field to increase linearly [$\Delta(h) = 24(h/h_c)$ meV] up to h_c, while it remains a constant [$\Delta(h)$ = 24 meV] above h_c. In Fig. 4A, in the low carrier density region, the conductivity shows a concave curve, as shown in the result for $n \sim 6.9 \times 10^{19}$ cm^{-3} (the green shaded regions in the conductivity curve). In addition, in some cases, it shows sign changes of the anomalous Hall conductivity with increasing h, as in the case of $n = 7.4 \times 10^{19}$ cm^{-3}. Our results also show sign changes of the nonlinear part with increasing carrier density, as shown by the curves for larger n. To see

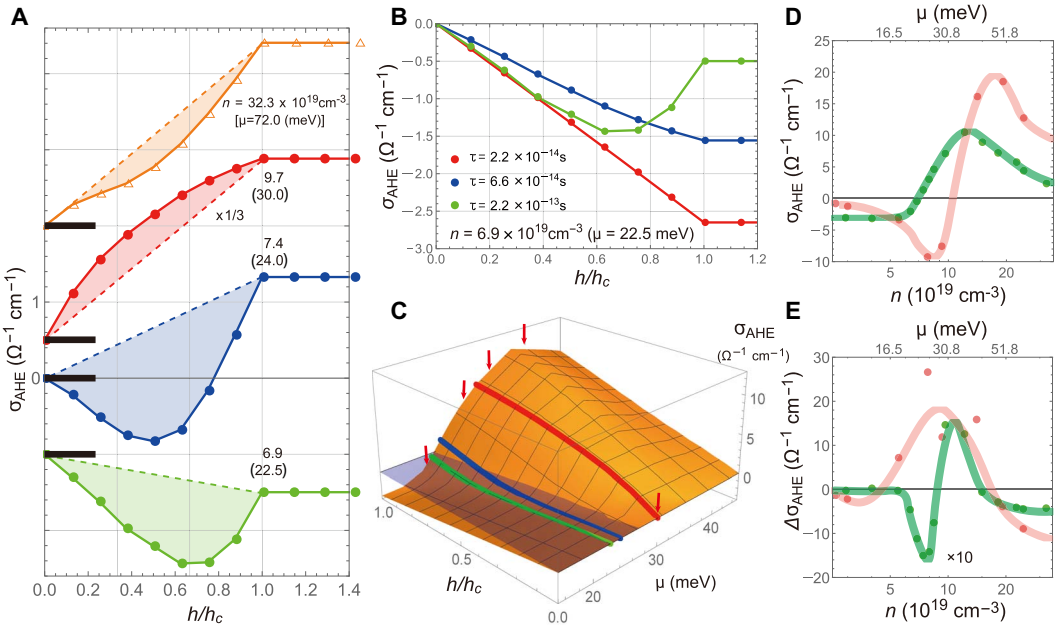

Fig. 4. Anomalous Hall conductivity of the effective Hamiltonian. (**A**) Field dependence of the anomalous Hall conductivity σ_{xy} for $\theta = -\pi/4$ with different chemical potential μ (the corresponding carrier density n is also shown). The relaxation time is fixed to $\tau = 2.2 \times 10^{-13}$ s ($\hbar/\tau$ = 3 meV). We assumed that the Zeeman splitting Δ of the band is proportional to the magnetic field $\Delta(h) = 24h/h_c$ meV while it is a constant (Δ = 24 meV) above h_c. Curves are vertically offset, as denoted by horizontal bars. (**B**) Relaxation time dependence of σ_{xy} at μ = 24 meV. (**C**) Three-dimensional plot of σ_{xy} for different chemical potentials and fields h. The solid lines show the path that corresponds to the curves in (A), and the red arrows are the positions of the band crossings at $h = 0$ and at $h = h_c$. The right two figures show the carrier density n dependence of Hall conductivity: (**D**) σ_{AHE} at $h = h_c$ and (**E**) the maximum value of $\Delta\sigma_{\text{AHE}}$. Green dots are the results of theoretical calculation, and the red dots are experimental results for corresponding carrier density n. The lines are merely guides to the eye. All results are for t = 300 meV, $\delta t = -100$ meV, V_{tetra} = 45 meV, and $\theta = -\pi/4.\theta = -\pi/4$.

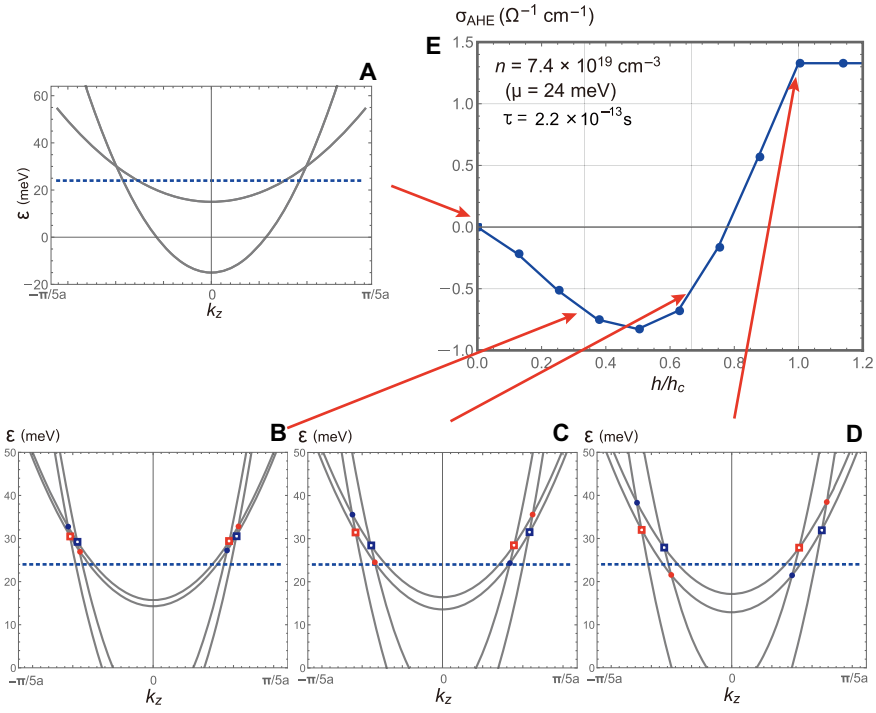

Fig. 5. Relation between the band structure and anomalous Hall conductivity. (**A** to **D**) The band structure of the Luttinger model at $h = 0$ (A), $h = h_c/3$ (B), $h = 2h_c/3$ (C), and $h = h_c$ (D). The solid circles (open squares) denote the position of the Weyl (double Weyl) nodes; the red (blue) dots are for nodes with positive (negative) chirality. (**E**) Field dependence of anomalous Hall conductivity for chemical potential $\mu = 24$ meV. All results are for $t = 300$ meV, $\delta t = -100$ meV, $V_{tetra} = 45$ meV, and $\theta = -\pi/4$.

the n dependence of the nonlinear part of σ_{AHE}, we define $\Delta\sigma_{AHE}$ as the maximum of the convex/concave, in a similar way to $\Delta\rho_{AHE}$ above; it is shown in Fig. 4E, along with that in the experiment. We find that the $\Delta\sigma_{AHE}$ changes from negative to positive at around $n \sim 9.0 \times 10^{19}$ cm^{-3} ($\mu = 29$ meV) and from positive to negative at around $n \sim 1.7 \times 10^{20}$ cm^{-3} ($\mu = 45$ meV). Although the characteristic carrier densities of the sign changes do not match with the experimental results precisely, the theory and the experiment agree semiquantitatively.

We next turn to the relaxation time dependence of σ_{AHE}; we find that the Hall conductivity is highly sensitive to the relaxation time. In Fig. 4B, we show the results of the anomalous Hall conductivity at $n \sim 6.9 \times 10^{19}$ cm^{-3} ($\mu = 22.5$ meV). The nonlinear behavior with $\tau = 2.2 \times 10^{-13}$ s (high mobility) is almost lost in the case of $\tau = 6.6 \times 10^{-14}$ s and lower (low mobility). Here, $\tau = 1 \times 10^{-13}$ s corresponds to $\mu = 180$ cm^2 V^{-1} s^{-1} assuming free electron mass. These results suggest that a very clean sample is necessary for the observation of the nonlinear behavior of the AHE with respect to h. Indeed, while the nonmonotonic curve of σ_{AHE} appears in the wide range of carrier density in the MBE films, such behavior was hardly observed in the previous samples by PLD (*14*).

These features found in the theoretical calculations are likely to be the consequences of multiband nature, in particular, the unusual structure of the Berry curvature due to the presence and movement of type II Weyl nodes in the conduction bands. As it is well known, the Weyl node is a drain (source) of the Berry curvature flux when it has a negative (positive) chirality, that is, the Berry curvature flows inward to (outward from) the Weyl node in the upper band when the node has negative (positive) chirality. On the other hand, the Berry curvature on the lower band has the opposite sign as the upper band, namely, $b^+(\vec{k}) = -b^-(\vec{k})$, where $b^+(\vec{k})$ and $b^-(\vec{k})$ are the Berry curvatures at wave number $\vec{k}$ for the upper and lower bands, respectively. As the texture of the Berry curvatures for the upper and lower bands have opposite signs, the contribution from the upper and lower bands close to the Fermi surface cancels when both the upper and lower bands are below the Fermi level. Therefore, the contribution to the AHE only comes from the region where only the lower band is occupied. For the Weyl node noted in blue circle on the right-hand side of Fig. 5D, the z component of the Berry curvature is negative if the Fermi level is below the Weyl node while positive if above (see also fig. S5). As the anomalous Hall conductivity is proportional to the integral of Berry curvature over the Fermi sea, the contribution from the electron states around the Weyl node gives a negative contribution when the Fermi surface is below the node (Fig. 5B), while it will be positive when above (Fig. 5D). A similar argument on the pair node (the node at $-\vec{k}_W$, where $\vec{k}_W$ is the position of the Weyl node) shows that the pair node also gives the same contribution. As the Berry curvature in the vicinity of the Weyl nodes is very large, this contribution may become visible when the Fermi volume is small (and hence, the integral of the Berry curvature within the Fermi surface is small) such as in the La-doped semiconductors as in $EuTiO_3$.

This scenario may explain the nonmonotonic behavior of the Hall conductivity around $\mu \sim 24$ meV ($n = 7.4 \times 10^{19}$ cm^{-3}). In Fig. 5A, we show the band structure of the Luttinger Hamiltonian without the Zeeman splitting; the plot is for the $(0, 0, k_z)$ line. Because of the uniaxial anisotropy induced by the substrate, the fourfold degeneracy at the Γ point is lifted, forming two light and one heavy electron bands (both bands are doubly degenerate); these two bands cross at $E = \frac{2}{3} V_{tetra} = 30$ meV. With finite Zeeman splitting, the two bands further split into four, leaving eight band crossing points for the heavy and light bands along the $(0, 0, k_z)$ line. Figure 5 (B to D) shows the band structures for different Zeeman fields, $h = h_c/3$, $2h_c/3$, and h_c, respectively. The eight

crossing points shown by the circles and squares in Fig. 5 (B to D) are type II Weyl nodes (*32*, *33*); the red (blue) dots are the Weyl nodes with positive (negative) chirality, and the double Weyl nodes (the Weyl nodes with twice the charge of the ordinary Weyl nodes) with positive and negative chirality are shown by red and blue squares, respectively. As shown in Fig. 5E, the minimum of the Hall conductivity at $n = 7.4 \times 10^{19}$ cm^{-3} (μ = 24 meV) coincides with the h at which the Weyl nodes cross the Fermi surface, qualitatively consistent with the above argument.

For the chemical potentials above μ = 24 meV, multiple Weyl nodes and the structure of the Berry curvature around them are also expected to contribute to the Hall conductivity. Complex structures of the anomalous Hall conductivity in Fig. 4 (A and C) appear around the Weyl nodes. This is also confirmed by calculating the Berry curvature on each band; we find a complex structure of the Berry curvature especially on the second and third bands where six Weyl nodes are located close by (fig. S5).

DISCUSSION

To conclude, we have investigated magnetotransport properties of La-doped ETO films on LSAT substrates. The mobilities of MBE films are one order of magnitude higher than those of PLD films. The carrier density dependence of the AHE is explained by the band crossing points induced by the epitaxial compressive strain from the substrate. In the AHE, an additional term that is not proportional to the magnetization curve can always be observed for MOMBE films. Such a nonlinear term could be rarely found for PLD films. Model calculations reveal that the change of Zeeman energy splitting during the magnetization process causes the nonmonotonic behavior of the AHE as a function of magnetic field. Because of the long scattering time of high-mobility MOMBE films, the effect of the Zeeman energy splitting on the AHE can be observed. These new findings strongly suggest that the electron-doped ETO film with high mobility is an ideal magnetic semiconductor to explore magnetotransport phenomena attributed to the Berry curvature of the simple band structure near $k = 0$.

Note that in preparing this article, we noticed a related paper by Ahadi *et al.* (*34*). They attribute the origin of the additional anomalous Hall resistivity to the topological Hall effect, which is different from our conclusion.

MATERIALS AND METHODS

Sample fabrication

Eu and La were provided from conventional effusion cells with each pure elemental source. For the Ti source, TTIP (99.9999%) was supplied from an MO container kept around 100°C without any carrier gas. Eu flux was kept at a beam equivalent pressure of 8×10^{-8} torr, and the rate of TTIP was varied to optimize the TTIP/Eu ratio. La flux was controlled by the temperature of the effusion cell that was calibrated by a quartz crystal microbalance flux monitor. $Eu_2Ti_2O_7$ with Eu^{3+} phase was more stable than perovskite $EuTiO_3$ with Eu^{2+} phase (*35*). To avoid oxidation to the $Eu_2Ti_2O_7$ phase, the films were grown in a base pressure of 2×10^{-8} torr. $EuTiO_3$ can be grown while supplying no intentional oxidation gas because of the four oxygen atoms incorporated per Ti in TTIP and epitaxial stabilization from the perovskite substrate LSAT. However, such insufficient oxidation conditions create a certain amount of oxygen vacancies in the films, doping electron carriers (~2×10^{19} cm^{-3}) even without La doping, as discussed in Fig. 1E.

Effective Hamiltonian

As the effective Hamiltonian for the Ti electrons, we considered the Luttinger model used in a precedent work (*14*). As the coupling term between the Eu moments and Ti electrons, we considered the couplings to the ferromagnetic moment ($\vec{h}$) and Neel order parameter ($\vec{n}$). The allowed coupling terms were determined from the symmetry analysis assuming cubic symmetry for $EuTiO_3$; as the uniaxial distortion from the substrate was very small, we assume that the change of the coupling constants due to the distortion is negligible. As both $\vec{h}$ and $\vec{n}$ are odd under time-reversal operation, we considered the matrices that are time-reversal odd. They are (*36*)

$$J_x, J_x^3, J_y, J_y^3, J_z, J_z^3 \tag{3A}$$

$$\left\{J_x, J_y^2 - J_z^2\right\}, \left\{J_y, J_z^2 - J_x^2\right\}, \left\{J_z, J_x^2 - J_y^2\right\}, J_xJ_yJ_z + J_zJ_yJ_x \tag{3B}$$

It is known that the ferromagnetic moments only couples to the six terms in Eq. 3A (*30*). Therefore, the general coupling term reads

$$H_{\mathrm{FM}} = \sum_{\alpha} \frac{h_\alpha}{3}\left(\cos\theta J_\alpha + \sin\theta J_\alpha\right).$$

In the main text, we only consider the magnetic moments along z axis. Hence, we defined $h = h_z$. On the other hand, a similar analysis shows that the Neel order parameter does not couple to any of the matrices in Eq. 3A and 3B. Therefore, in the main text, we only consider the coupling term for the ferromagnetic moments.

SUPPLEMENTARY MATERIALS

Supplementary material for this article is available at http://advances.sciencemag.org/cgi/content/full/4/7/eaar7880/DC1

Section S1. Optimization of the growth condition of $EuTiO_3$ films by changing the flux ratio between TTIP and Eu

Section S2. Temperature dependence of magnetization

Section S3. Anomalous Hall conductivity σ_{xy} for La-doped ETO films

Section S4. Berry curvature distribution of the Luttinger model

Fig. S1. Structure characterizations of $EuTiO_3$ films on LSAT (001) substrates grown at various TTIP/Eu ratios.

Fig. S2. Tetragonal distortion of $EuTiO_3$ film on LSAT (001) substrate.

Fig. S3. Magnetization property.

Fig. S4. Magnetic field dependence of anomalous Hall conductivity.

Fig. S5. Band structure and Berry curvature.

REFERENCES AND NOTES

1. S. Maekawa, *Concepts in Spin Electronics* (Oxford Univ., 2006).
2. R. Karplus, J. M. Luttinger, Hall effect in ferromagnetics. *Phys. Rev.* **95**, 1154–1160 (1954).
3. J. Smit, The spontaneous Hall effect in ferromagnetics II. *Physica* **24**, 39–51 (1958).
4. L. Berger, Side-jump mechanism for the Hall effect of ferromagnets. *Phys. Rev. B* **2**, 4559–4566 (1970).
5. Y. Taguchi, Y. Oohara, H. Yoshizawa, N. Nagaosa, Y. Tokura, Spin chirality, Berry phase, and anomalous Hall effect in a frustrated ferromagnet. *Science* **291**, 2573–2576 (2001).
6. N. Nagaosa, J. Sinova, S. Onoda, A. H. MacDonald, N. P. Ong, Anomalous Hall effect. *Rev. Mod. Phys.* **82**, 1539–1592 (2010).
7. J. Ye, Y. B. Kim, A. J. Millis, B. I. Shraiman, P. Majumdar, Z. Tešanović, Berry phase theory of the anomalous Hall effect: Application to colossal magnetoresistance manganites. *Phys. Rev. Lett.* **83**, 3737–3740 (1999).
8. S. H. Chun, M. B. Salamon, Y. Lyanda-Geller, P. M. Goldbart, P. D. Han, Magnetotransport in manganites and the role of quantal phases: Theory and experiment. *Phys. Rev. Lett.* **84**, 757–760 (2000).

9. T. Jungwirth, Q. Niu, A. H. MacDonald, Anomalous Hall effect in ferromagnetic semiconductors. *Phys. Rev. Lett.* **88**, 207208 (2002).
10. M. Onoda, N. Nagaosa, Topological nature of anomalous Hall effect in ferromagnets. *J. Phys. Soc. Jpn.* **71**, 19–22 (2002).
11. Z. Fang, N. Nagaosa, K. S. Takahashi, A. Asamitsu, R. Mathieu, T. Ogasawara, H. Yamada, M. Kawasaki, Y. Tokura, K. Terakura, The anomalous Hall effect and magnetic monopoles in momentum space. *Science* **302**, 92–95 (2003).
12. W.-L. Lee, S. Watauchi, V. L. Miller, R. J. Cava, N. P. Ong, Dissipationless anomalous Hall current in the ferromagnetic spinel $CuCr_2Se_{4-x}Br_x$. *Science* **303**, 1647–1649 (2004).
13. Y. Yao, L. Kleinman, A. H. MacDonald, J. Sinova, T. Jungwirth, D.-S. Wang, E. Wang, Q. Niu, First principles calculation of anomalous Hall conductivity in ferromagnetic bcc Fe. *Phys. Rev. Lett.* **92**, 037204 (2004).
14. K. S. Takahashi, M. Onoda, M. Kawasaki, N. Nagaosa, Y. Tokura, Control of the anomalous Hall effect by doping in $Eu_{1-x}La_xTiO_3$ thin films. *Phys. Rev. Lett.* **103**, 057204 (2009).
15. A. P. Petrović, Y. Kato, S. S. Sunku, T. Ito, P. Sengupta, L. Spalek, M. Shimuta, T. Katsufuji, C. D. Batista, S. S. Saxena, C. Panagopoulos, Electric field modulation of the tetragonal domain orientation revealed in the magnetic ground state of quantum paraelectric $EuTiO_3$. *Phys. Rev. B* **87**, 064103 (2013).
16. M. A. Ruderman, C. Kittel, Indirect exchange coupling of nuclear magnetic moments by conduction electrons. *Phys. Rev.* **96**, 99 (1954).
17. T. Kasuya, A theory of metallic ferro- and antiferromagnetism on Zener's model. *Prog. Theor. Phys.* **16**, 45–57 (1956).
18. K. Yosida, Magnetic properties of Cu-Mn alloys. *Phys. Rev.* **106**, 893–898 (1957).
19. J. Son, P. Moetakef, B. Jalan, O. Bierwagen, N. J. Wright, R. Engel-Herbert, S. Stemmer, Epitaxial $SrTiO_3$ films with electron mobilities exceeding 30,000 $cm^2 V^{-1} s^{-1}$. *Nat. Mater.* **9**, 482–484 (2010).
20. Y. Matsubara, K. S. Takahashi, M. S. Bahramy, Y. Kozuka, D. Maryenko, J. Falson, A. Tsukazaki, Y. Tokura, M. Kawasaki, Observation of the quantum Hall effect in δ-doped $SrTiO_3$. *Nat. Commun.* **7**, 11631 (2016).
21. Y. Matsubara, K. S. Takahashi, Y. Tokura, M. Kawasaki, Single-crystalline $BaTiO_3$ films grown by gas-source molecular beam epitaxy. *Appl. Phys. Express* **7**, 125502 (2014).
22. K. Shimamoto, K. Hatabayashi, Y. Hirose, S. Nakao, T. Fukumura, T. Hasegawa, Full compensation of oxygen vacancies in $EuTiO_3$ (001) epitaxial thin film stabilized by a $SrTiO_3$ surface protection layer. *Appl. Phys. Lett.* **102**, 042902 (2013).
23. S. Onoda, N. Sugimoto, N. Nagaosa, Intrinsic versus extrinsic anomalous Hall effect in ferromagnets. *Phys. Rev. Lett.* **97**, 126602 (2006).
24. T. Fukumura, H. Toyosaki, K. Ueno, M. Nakano, T. Yamasaki, M. Kawasaki, A scaling relation of anomalous Hall effect in ferromagnetic semiconductors and metals. *Jpn. J. Appl. Phys.* **46**, L642 (2007).
25. A. Neubauer, C. Pfleiderer, B. Binz, A. Rosch, R. Ritz, P. G. Niklowitz, P. Böni, Topological Hall effect in the A phase of MnSi. *Phys. Rev. Lett.* **102**, 186602 (2009).
26. N. Kanazawa, Y. Onose, T. Arima, D. Okuyama, K. Ohoyama, S. Wakimoto, K. Kakurai, S. Ishiwata, Y. Tokura, Large topological Hall effect in a short-period helimagnet MnGe. *Phys. Rev. Lett.* **106**, 156603 (2011).
27. J. Matsuno, N. Ogawa, K. Yasuda, F. Kagawa, W. Koshibae, N. Nagaosa,Y. Tokura, M. Kawasaki, Interface-driven topological Hall effect in $SrRuO_3$-$SrIrO_3$ bilayer. *Sci. Adv.* **2**, e1600304 (2016).
28. S. A. Montoya, S. Couture, J. J. Chess, J. C. T. Lee, N. Kent, D. Henze, S. K. Sinha, M.-Y. Im, S. D. Kevan, P. Fischer, B. J. McMorran, V. Lomakin, S. Roy, E. E. Fullerton, Tailoring magnetic energies to form dipole skyrmions and skyrmion lattices. *Phys. Rev. B* **95**, 024415 (2017).
29. N. Nagaosa, Y. Tokura, Topological properties and dynamics of magnetic skyrmions. *Nat. Nanotechnol.* **8**, 899–911 (2013).
30. A. Abragam, B. Bleaney, *Electron Paramagnetic Resonance of Transition Ions* (Clarendon Press, 1970).
31. J. M. Luttinger, Quantum theory of cyclotron resonance in semiconductors: General theory. *Phys. Rev.* **102**, 1030 (1956).
32. A. A. Soluyanov, D. Gresch, Z. Wang, Q. Wu, M. Troyer, X. Dai, B. A. Bernevig, Type-II Weyl semimetals. *Nature* **527**, 495–498 (2015).
33. Y. Xu, F. Zhang, C. Zhang, Structured Weyl points in spin-orbit coupled Fermionic superfluids. *Phys. Rev. Lett.* **115**, 265304 (2015).
34. K. Ahadi, L. Galletti, S. Stemmer, Evidence of a topological Hall effect in $Eu_{1-x}Sm_xTiO_3$. *Appl. Phys. Lett.* **111**, 172403 (2017).
35. N. L. Henderson, J. Baek, P. S. Halasyamani, R. E. Schaak, Ambient-pressure synthesis of SHG-active $Eu_2Ti_2O_7$ with a [110] layered perovskite structure: Suppressing pyrochlore formation by oxidation of perovskite-type $EuTiO_3$. *Chem. Mater.* **19**, 1883–1885 (2007).
36. S. Murakami, N. Nagaosa, S.-C. Zhang, SU(2) non-Abelian holonomy and dissipationless spin current in semiconductors. *Phys. Rev. B* **69**, 235206 (2004).

Acknowledgments

Funding: This work was partly supported by the "Funding Program for World-Leading Innovative R&D on Science and Technology (FIRST)" of the Japan Society for the Promotion of Science initiated by the Council for Science and Technology Policy, JSPS KAKENHI (No. JP16H06717, JP18H03676, JP18H04222, and JP26103006), ImPACT Program of Council for Science, Technology and Innovation (Cabinet office, Government of Japan), CREST-JST (no. JPMJCR16F1), and PRESTO-JST "Innovative nanoelectronics through interdisciplinary collaboration among material, device and system layers." **Author contributions:** K.S.T., T.M., and Q.Y.W. grew and characterized the films. K.S.T. and T.M. analyzed the data. H.I. did the theoretical calculations. Y.T., N.N., and M.K. contributed to the discussion of the results and guided the project. K.S.T. and H.I. wrote the manuscript with contributions from all authors. **Competing interests:** The authors declare no competing interests. **Data and materials availability:** All data needed to evaluate the conclusions in the paper are present in the paper and/or the Supplementary Materials. Additional data related to this paper may be requested from the authors.

Submitted 21 December 2017
Accepted 11 June 2018
Published 20 July 2018
10.1126/sciadv.aar7880

Citation: K. S. Takahashi, H. Ishizuka, T. Murata, Q. Y. Wang, Y. Tokura, N. Nagaosa, M. Kawasaki, Anomalous Hall effect derived from multiple Weyl nodes in high-mobility $EuTiO_3$ films. *Sci. Adv.* **4**, eaar7880 (2018).

ScienceAdvances

Anomalous Hall effect derived from multiple Weyl nodes in high-mobility $EuTiO_3$ films

Kei S. Takahashi, Hiroaki Ishizuka, Tomoki Murata, Qing Y. Wang, Yoshinori Tokura, Naoto Nagaosa and Masashi Kawasaki

Sci Adv **4** (7), eaar7880.
DOI: 10.1126/sciadv.aar7880